

# A 3D GBSM for Ship-to-Land Communications

Yubei He<sup>1</sup>, Hengtai Chang<sup>1</sup>, Yu Liu<sup>1</sup>, Wensheng Zhang<sup>1</sup>, Jian Sun<sup>1</sup>, and Cheng-Xiang Wang<sup>2,3</sup>

<sup>1</sup>Shandong Provincial Key Lab of Wireless Communication Technologies,  
School of Information Science and Engineering, Shandong University, Qingdao, Shandong, 266237, China.

<sup>2</sup>National Mobile Communications Research Laboratory,  
School of Information Science and Engineering, Southeast University, Nanjing, Jiangsu, 210096, China.

<sup>3</sup>Purple Mountain Laboratories, Nanjing, Jiangsu, 211111, China.  
Email: {heyubei, hunter\_chang}@126.com, xinwenliuyu@163.com,  
{zhangwsh, sunjian}@sdu.edu.cn, chxwang@seu.edu.cn

**Abstract**—In this paper, we propose a novel three-dimensional (3D) geometry-based stochastic model (GBSM) for single-input multiple-output (SIMO) maritime ship-to-land communication channels. The proposed model is a combination of a line-of-sight (LoS) component, a specular reflection component, and scattering components from a sphere model and multiple confocal elliptic-cylinder models. Based on the proposed model, some key statistical properties like space-time-correlation-function (STCF) and Doppler power spectrum density (PSD) are derived. The impacts of the moving direction angles on Doppler PSD and Ricean  $K$  factor on spatial cross-correlation function (CCF) are investigated. Finally, the consistency between the power delay profile (PDP) for the proposed simulation model and the measurement data demonstrates the validity of the proposed model.

**Index Terms**—Maritime ship-to-land communications, SIMO channel model, GBSM, channel characteristics

## I. INTRODUCTION

In recent years, rapid evolution has taken place in every aspect of terrestrial communications which leads to great changes on people's daily life. However, in maritime communication field, the needs of fishery industry and maritime security have not been satisfied entirely [1]. The most existing ways of maritime communications are satellite communications and very high frequency (VHF) communication systems which are highly costly or have low bandwidth and capacity [2]. To support future communication systems and optimize the communication links, the characteristics of the channels over the sea should be investigated.

Compared with the terrestrial communications, the environments of maritime communications are lacking scatterers generally. Due to the reflection of sea water, the main components of received power can include a strong specular reflection component besides the LoS component. In addition, the vagaries of climate will cause attenuation, and the motion of wave will lead to the roughness of sea surface which impacts the channel performance through scattering.

With regard to the channel characteristics of maritime communications, many researches of channel measurements and modelling have been carried out [2]–[16]. In [3]–[8], some channel characteristics over the sea were measured in different situations such as ship-to-land communications or ship-to-ship communications using different frequencies, and some empirical models were obtained in [4], [5]. In [9], [10],

the deterministic or quasi-deterministic models were proposed to describe the path loss in electromagnetic wave propagation. In [2], [11], the ray-tracing method was used to model the channels and study the feasibility of millimeter wave band. However, these kinds of channel models are not flexible to describe general maritime communication environments. In [12], the maritime channels were studied based on the finite difference time domain (FDTD) method. This method can improve the accuracy of the models by using the spectra of sea waves to generate the sea surface, but it was limited because of the huge calculation complexity and physical memory requirement. Therefore it cannot simulate the channels at long distances. The literature [13], [14] tried to use GBSMs to explore the characteristics of ship-to-ship channel. Besides the basic communication links from sea surface, the literature [15], [16] proposed that the refraction path, which caused by evaporation duct, should be taken into consideration. Since evaporation duct is greatly affected by climate, it does not exist everywhere and generally appears when communication distances are long.

However, the models mentioned in the preceding literature are two-dimensional (2D). As a result, the scattering effect caused by the fluctuation of sea level and the buildings around the antennas on the shore was seldom considered in previous channel models. In addition, most of the existing work only focused on the large-scale fading characteristics like path loss, while the small-scale statistical properties were rarely discussed. To fill these gaps, we propose a novel 3D GBSM to describe the ship-to-land channels. For the maritime communication scenarios, especially for the short range communication, the scattering from the buildings near the coast cannot be ignored. In order to describe the scattering, we assume that the scatterers are distributed on surface of a sphere centered on the receiving antennas which are mounted near the shore. Because the sea surface is a undulating surface rather than a stationary horizontal plane, multiple confocal elliptic-cylinders with low height were used to describe the distribution of scatterers for scattering from the rough sea surface.

The rest of this paper is organized as follows. In Section II, the details of the novel 3D theoretical GBSM are described. At the same time, the reference model and simulation model are derived. Section III analyzes some important channel characteristics based on the proposed model. In Section IV, the

simulation results and analysis are given. Finally, conclusions are drawn in Section V.

## II. A 3D THEORETICAL GBSM

### A. Description of the 3D SIMO reference model

For the maritime communication scenario illustrated by Fig. 1, the receiver (Rx) is located on the shore, so it is fixed. The transmitter (Tx) is equipped on board, thus it moves with ship. The velocity of the Tx is expressed by  $v$ . In order to describe the moving direction of Tx, we use  $\gamma$  to indicate its azimuth angle between the velocity vector  $v$  and the  $y$  axis. Since ship can only move on the sea surface, we do not need to discuss its elevation angles. In order to match our model with the actual situation well, the SIMO communication system with  $M$  antenna elements at Rx and one antenna element at Tx is chosen. Because the coastlines are generally long, it is easier to set multiple antennas on shore, while it is difficult on boats. In this paper, we assume a  $1 \times 2$  SIMO channel, i.e.,  $M = 2$ , to simplify the calculations. The number of antennas can be increased to construct a larger antenna array.

The proposed model is the combination of a LoS component, a reflection component, and scattering components. The scattering components include single-bounced rays from the sphere model and the multiple confocal elliptic-cylinder models, respectively, and double-bounced rays through the sphere model and the multiple confocal elliptic-cylinder models. We assume there are  $N_1$  scatterers lying on the sphere model with radius  $R$  (denoted by  $s^{(n_1)}$ ) to represent the effect of the buildings around the Rx. In order to represent the effect of fluctuating ocean surface in different ranges,  $L$  confocal elliptic-cylinders taking the projection of transceivers to  $x$ - $y$  plane as focal points and with different major axis lengths (denoted by  $a(l)$ ) are adopted. Similarly, we assume there are  $N_2$  scatterers lying on every elliptic-cylinder (denoted by  $s^{(l,n_2)}$ ). In addition, the appropriate height of elliptic-cylinders can be chosen according to height of sea wave. The main parameters in the proposed model are defined in Table I.

For the 3D SIMO channel, we use  $q$  ( $q = 1, \dots, M$ ) to denote the antenna elements of Rx, and  $p$  to denote Tx. According to the proposed model, the complex impulse response of the fading channel between the Tx and  $q$ th Rx can be expressed as

$$\begin{aligned} h_{pq}(t, \tau') &= h_{pq}^{\text{LoS}}(t)\delta(\tau' - \tau'_{\text{LoS}}) + h_{pq}^{\text{Ref}}(t)\delta(\tau' - \tau'_{\text{Ref}}) \\ &+ h_{pq}^{\text{SB1}}(t)\delta(\tau' - \tau'_{\text{SB1}}) + h_{pq}^{\text{SB2}}(t)\delta(\tau' - \tau'_{\text{SB2}}) \\ &+ h_{pq}^{\text{DB}}(t)\delta(\tau' - \tau'_{\text{DB}}) \end{aligned} \quad (1)$$

where

$$\begin{aligned} h_{pq}^{\text{LoS}}(t) &= \sqrt{\frac{K}{K+1}} e^{-j2\pi f_c \frac{d_{\text{LoS}}}{c}} \\ &\times e^{j2\pi f_{Tmax} t \cos(\alpha_T^{\text{LoS}} - \gamma) \cos(\beta_T^{\text{LoS}})} \end{aligned} \quad (2a)$$

$$\begin{aligned} h_{pq}^{\text{Ref}}(t) &= \sqrt{\frac{\eta_{\text{Ref}}}{K+1}} e^{-j(\psi_{\text{Ref}} + 2\pi f_c \frac{d_{\text{Ref}}}{c})} \\ &\times e^{j2\pi f_{Tmax} t \cos(\alpha_T^{\text{Ref}} - \gamma) \cos(\beta_T^{\text{Ref}})} \end{aligned} \quad (2b)$$

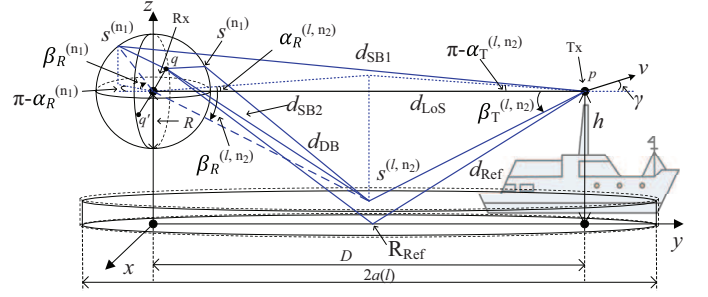


Fig. 1. The proposed 3D SIMO GBSM combining a sphere model and multiple confocal elliptic-cylinder models (The ratio in the figure is just for intuitionistic description).

$$\begin{aligned} h_{pq}^{\text{SB1}}(t) &= \sqrt{\frac{\eta_{\text{SB1}}}{K+1}} \lim_{N_1 \rightarrow \infty} \sum_{n_1=1}^{N_1} \frac{1}{\sqrt{N_1}} \\ &\times e^{-j(\psi_{n_1} + 2\pi f_c \frac{d_{\text{SB1}}^{(n_1)}}{c})} \\ &\times e^{j2\pi f_{Tmax} t \cos(\alpha_T^{(n_1)} - \gamma) \cos(\beta_T^{(n_1)})} \end{aligned} \quad (2c)$$

$$\begin{aligned} h_{pq}^{\text{SB2}}(t) &= \sqrt{\frac{\eta_{\text{SB2}}}{K+1}} \lim_{N_2 \rightarrow \infty} \sum_{l=1}^L \sum_{n_2=1}^{N_2} \frac{1}{\sqrt{LN_2}} \\ &\times e^{-j(\psi_{l,n_2} + 2\pi f_c \frac{d_{\text{SB2}}^{(l,n_2)}}{c})} \\ &\times e^{j2\pi f_{Tmax} t \cos(\alpha_T^{(l,n_2)} - \gamma) \cos(\beta_T^{(l,n_2)})} \end{aligned} \quad (2d)$$

$$\begin{aligned} h_{pq}^{\text{DB}}(t) &= \sqrt{\frac{\eta_{\text{DB}}}{K+1}} \lim_{N_1, N_2 \rightarrow \infty} \sum_{l=1}^L \sum_{n_1=1}^{N_1} \sum_{n_2=1}^{N_2} \frac{1}{\sqrt{LN_1 N_2}} \\ &\times e^{-j(\psi_{l,n_1,n_2} + 2\pi f_c \frac{d_{\text{DB}}^{(l,n_1,n_2)}}{c})} \\ &\times e^{j2\pi f_{Tmax} t \cos(\alpha_T^{(l,n_2)} - \gamma) \cos(\beta_T^{(l,n_2)})}. \end{aligned} \quad (2e)$$

Here,  $h_{pq}^{\text{LoS}}(t)$  and  $h_{pq}^{\text{Ref}}(t)$  denote the complex envelopes of the LoS component and the reflection component, respectively. The complex envelope of the single-bounced rays of the path Tx- $s^{(n_1)}$ -Rx are expressed by  $h_{pq}^{\text{SB1}}(t)$ , the complex envelope of the single-bounced rays of the path Tx- $s^{(l,n_2)}$ -Rx are represented by  $h_{pq}^{\text{SB2}}(t)$ , and  $h_{pq}^{\text{DB}}(t)$  indicates the complex envelope of the double-bounced rays of the path Tx- $s^{(l,n_2)}$ - $s^{(n_1)}$ -Rx. Note that  $\tau'_i = \frac{d_i}{c}$  ( $i = \text{LoS, Ref, SB1}^{(n_1)}, \text{SB2}^{(l,n_2)}, \text{DB}^{(l,n_1,n_2)}$ ) denotes the delay of each ray. In our model, only the small-scale fading is considered, so the total received power is normalized to 1. In the above equations,  $K$  is the Ricean factor and the total reflected and scattered power is  $1/(K+1)$ ,  $c$  is the speed of light,  $f_c$  is the carrier frequency, and  $f_{Tmax} = \frac{v f_c}{c}$  is the maximum Doppler frequency caused by the movement of the Tx. To determine the power proportions of single- and double-bounced rays, we set  $\eta_{\text{Ref}}, \eta_{\text{SB1}}, \eta_{\text{SB2}}$ , and  $\eta_{\text{DB}}$  to be power-related coefficients and their summation is 1. The random phase shifts  $\psi_{\text{Ref}}, \psi_{n_1}, \psi_{l,n_2}$ , and  $\psi_{l,n_1,n_2}$  are independent

and identically distributed (i.i.d.) random variables which are uniformly distributed over  $(0, 2\pi]$ .

Based on the geometrical relationship and the law of cosines, the distance of each ray can be derived as,

$$d_{\text{LoS}} \approx D + \frac{\delta_R}{2} \cos(\varphi_R) \cos(\theta_R) \quad (3a)$$

$$d_{\text{Ref}} \approx \sqrt{4h^2 + D^2} + \frac{\delta_R}{2} \cos(A) \quad (3b)$$

$$d_{\text{SB1}}^{(n_1)} \approx d_{ps^{(n_1)}} + R + \frac{\delta_R}{2} \cos(B^{(n_1)}) \quad (3c)$$

$$d_{\text{SB2}}^{(l, n_2)} \approx d_{ps^{(l, n_2)}} + d_{s^{(l, n_2)}q} + \frac{\delta_R}{2} \cos(B^{(l, n_2)}) \quad (3d)$$

$$d_{\text{DB}}^{(l, n_1, n_2)} \approx d'_{ps^{(l, n_2)}} + d_{s^{(l, n_2)}s^{(n_1)}} + R + \frac{\delta_R}{2} \cos(B^{(n_1)}) \quad (3e)$$

where

$$d_{ps^{(n_1)}} = \sqrt{R^2 + D^2 - 2RD \cos(\beta_R^{(n_1)}) \cos(\alpha_R^{(n_1)})} \quad (4a)$$

$$d_{s^{(l, n_2)}q} = \frac{4a^2(l) - D^2}{(4a(l) - 2D \cos \alpha_R^{(l, n_2)}) \cos \beta_R^{(l, n_2)}} \quad (4b)$$

$$d_{ps^{(l, n_2)}} = \sqrt{d_{s^{(l, n_2)}q}^2 + D^2 - 2d_{s^{(l, n_2)}q} D \cos \beta_R^{(l, n_2)} \cos \alpha_R^{(l, n_2)}} \quad (4c)$$

$$d_{s^{(l, n_2)}s^{(n_1)}} = \sqrt{(d_1^{(l, n_1, n_2)})^2 + (R \sin \beta_R^{(n_1)} - d'_{ps^{(l, n_2)}} \sin \beta_T^{(l, n_2)})^2} \quad (4d)$$

$$d'_{ps^{(l, n_2)}} = \frac{4a^2(l) - D^2}{(4a(l) + 2D \cos \alpha_T^{(l, n_2)}) \cos \beta_T^{(l, n_2)}} \quad (4e)$$

$$(d_1^{(l, n_1, n_2)})^2 = (d_2^{(l, n_2)})^2 + R^2 \cos^2 \beta_R^{(n_1)} - 2d_2^{(l, n_2)} R \cos \beta_R^{(n_1)} \cos(C^{(l, n_2)} + \alpha_R^{(n_1)}) \quad (4f)$$

$$d_2^{(l, n_2)} = 2a(l) - d'_{ps^{(l, n_2)}} \cos \beta_T^{(l, n_2)} \quad (4g)$$

$$C^{(l, n_2)} = \arccos \frac{D^2 + (d_2^{(l, n_2)})^2 - (d'_{ps^{(l, n_2)}})^2 \cos^2 \beta_T^{(l, n_2)}}{2Dd_2^{(l, n_2)}} \quad (4h)$$

$$\cos(A) = \frac{D}{\sqrt{4h^2 + D^2}} \cos(\varphi_R) \cos(\theta_R) - \frac{2h}{\sqrt{4h^2 + D^2}} \sin(\varphi_R) \quad (4i)$$

$$\cos(B^{(n_1)}) = \cos(\varphi_R) \cos(\beta_R^{(n_1)}) \cos(\theta_R - \alpha_R^{(n_1)}) + \sin(\varphi_R) \sin(\beta_R^{(n_1)}) \quad (4j)$$

TABLE I  
DEFINITION OF PARAMETERS.

Parameters	Definitions
$a(l)$ ( $l = 1, 2, \dots, L$ )	Semi-major axis length of the $l$ th confocal elliptic-cylinder
$D$	The distance between Tx and the center of Rx array
$h$	Altitude of TX and the center of Rx array relative to the horizontal plane
$\delta_R$	Antenna element spacing at the Rx
$R$	Radius of the sphere around the Rx
$\theta_R, \varphi_R$	Orientation of the Rx antenna array in the $x$ - $y$ plane and elevation of the Rx antenna array relative to the $x$ - $y$ plane, respectively
$\alpha_R^{\text{LoS}}, \beta_R^{\text{LoS}}$	AAoA/EAoA of the LoS component
$\alpha_R^{\text{Ref}}, \beta_R^{\text{Ref}}$	AAoA/EAoA of the reflection component
$\alpha/\beta_T^{(n_1)}, \alpha/\beta_R^{(n_1)}$	AAoDs/EAoDs and AAoAs/EAoAs of the scattering components from the $n_1$ th scatterers on the sphere model
$\alpha/\beta_T^{(l, n_2)}, \alpha/\beta_R^{(l, n_2)}$	AAoDs/EAoDs and AAoAs/EAoAs of the scattering components from the $n_2$ th scatterers on the $l$ th elliptic-cylinder model
$d_{\text{LoS}}, d_{\text{Ref}}, d_{\text{SB1}}, d_{\text{SB2}}, d_{\text{DB}}, d_{\text{AB}}$	Distances of LoS component, reflection component, single-bounced, double-bounced scattering components, and distance between A and B
$R_{\text{Ref}}$	Reflection point

$$\cos(B^{(l, n_2)}) = \cos(\varphi_R) \cos(\beta_R^{(l, n_2)}) \cos(\theta_R - \alpha_R^{(l, n_2)}) + \sin(\varphi_R) \sin(\beta_R^{(l, n_2)}) \quad (4k)$$

It is noted that for (3a)-(3e), small angle approximations are adopted in cosine functions ( $\cos(x) \approx 1$ , when  $x$  is small) to simplify the calculation.

In the above formulas, the values of the azimuth/elevation angles of departure (AAoDs/EAoDs) and the azimuth/elevation angles of arrival (AAoAs/EAoAs) are discrete. If there are infinite scatterers on every geometric model (i.e.,  $N_1, N_2 \rightarrow \infty$ ), the angles can be seen as random variables represented by  $\alpha_R^{(1)}/\beta_R^{(1)}$ ,  $\alpha_T^{(1)}/\beta_T^{(1)}$ ,  $\alpha_R^{(l, 2)}/\beta_R^{(l, 2)}$ , and  $\alpha_T^{(l, 2)}/\beta_T^{(l, 2)}$ . For the single-bounced components of the path Tx- $s^{(n_1)}$ -Rx, the relationship between the AoDs and AoAs can be expressed as  $\alpha_T^{(n_1)} = (\pi - \arccos(\frac{2D^2 - 2RD \cos \beta_R^{(n_1)} \cos \alpha_R^{(n_1)}}{2D \sqrt{R^2 \cos^2 \beta_R^{(n_1)} + D^2 - 2DR \cos \beta_R^{(n_1)} \cos \alpha_R^{(n_1)}}})) \text{sgn}(\alpha_R^{(n_1)})$ ,  $\beta_T^{(n_1)} = \arcsin(\frac{R \sin \beta_R^{(n_1)}}{\sqrt{R^2 + D^2 - 2DR \cos \beta_R^{(n_1)} \cos \alpha_R^{(n_1)}}})$ , where  $\text{sgn}(\cdot)$  is the sign function. As for the single-bounced components of the path Tx- $s^{(l, n_2)}$ -Rx, the relationship between the AoDs and AoAs are  $\alpha_T^{(l, n_2)} = (\pi - \arccos(\frac{D^2 + d_{ps^{(l, n_2)}}^2 \cos^2 \beta_R^{(l, n_2)} - d_{s^{(l, n_2)}q}^2 \cos^2 \beta_T^{(l, n_2)}}{2D d_{ps^{(l, n_2)}} \cos \beta_R^{(l, n_2)}})) \text{sgn}(\alpha_R^{(l, n_2)})$ ,  $\beta_T^{(l, n_2)} = \arcsin(\frac{d_{s^{(l, n_2)}q} \sin \beta_R^{(l, n_2)}}{d_{ps^{(l, n_2)}}})$ . As a result, we only determine the distribution of the AAoAs/EAoAs for single-bounced rays. For the AAoAs/EAoAs of scatterers on the sphere model and AAoAs of scatterers on the multiple confocal elliptic-cylinder models, the distribution of them

can be assumed as von-Mises distribution [17], [18] with different mean angles  $x_0$  and different values of concentration parameter  $k$  which describes the spread of the data,

$$f(x) = \frac{e^{k \cos(x-x_0)}}{2\pi I_0(k)}, -\pi \leq x < \pi, k \geq 0 \quad (5)$$

where  $I_0(\cdot)$  is the zeroth-order modified Bessel function of the first kind,  $x_0 \in [-\pi, \pi)$ .

As for the distribution of the EAOAs for scatterers lying on the multiple confocal elliptic-cylinder models, we choose the cosine distribution because it can limit the angles to a certain extent according to the height of the models. This distribution can be given by

$$f(\beta) = \frac{1}{2\beta_s} [1 + \cos(\frac{\pi(\beta - \beta_0)}{\beta_s})], \beta_0 - \beta_s \leq \beta \leq \beta_0 + \beta_s \quad (6)$$

where  $\beta_0$  is the mean value and  $\beta_s$  is the scale parameter to determine the range.

In addition, the AAOAs/EAOAs and AAOds/EAOds of the LoS component and reflection component are  $\alpha_R^{\text{LoS}} \approx \beta_R^{\text{LoS}} \approx \beta_T^{\text{LoS}} \approx 0$ ,  $\alpha_T^{\text{LoS}} \approx \pi$ ,  $\alpha_R^{\text{Ref}} \approx 0$ ,  $\beta_R^{\text{Ref}} \approx -\arctan(\frac{2h}{D})$ ,  $\beta_T^{\text{Ref}} \approx \arctan(\frac{2h}{D}) - \pi$ , and  $\alpha_T^{\text{Ref}} \approx \pi$  [19]. For double-bounced rays, we assume that the AAOds and AAOAs/EAOAs follow von-Mises distribution, and the EAOds follow cosine distribution in the same way as above.

### B. Description of the 3D SIMO simulation model

The reference model is based on the assumption that there are infinite scatterers on the geometric models. However, this assumption leads to tremendous computational complexity. To facilitate simulation and calculation, the sum of sinusoids (SoS) method can be used to built a simulation model with finite numbers of scatterers (i.e.,  $N_1, N_2$ ) based on the reference model. Hence, the AAOds/EAOds, AAOAs/EAOAs and the random phase shifts should be discretized and they still follow the same distributions as those in the reference model.

At this point, the complex impulse response of the fading channel can be expressed as

$$\begin{aligned} \tilde{h}_{pq}(t, \tau') &= \tilde{h}_{pq}^{\text{LoS}}(t, \tau') + \tilde{h}_{pq}^{\text{Ref}}(t, \tau') + \tilde{h}_{pq}^{\text{SB1}}(t, \tau') \\ &+ \tilde{h}_{pq}^{\text{SB2}}(t, \tau') + \tilde{h}_{pq}^{\text{DB}}(t, \tau'). \end{aligned} \quad (7)$$

In  $\tilde{h}_{pq}^{\text{LoS}}(t, \tau')$ ,  $\tilde{h}_{pq}^{\text{Ref}}(t, \tau')$ ,  $\tilde{h}_{pq}^{\text{SB1}}(t, \tau')$ ,  $\tilde{h}_{pq}^{\text{SB2}}(t, \tau')$ , and  $\tilde{h}_{pq}^{\text{DB}}(t, \tau')$ , the numbers of scatterers are finite.

## III. STATISTICAL PROPERTIES OF THE 3D GBSM

### A. STCF

STCF can be used to describe the correlation characteristics between the received complex envelopes  $h_{pq}^m(t)$  and  $h_{pq'}^m(t)$  ( $m = \text{LoS, Ref, SB1, SB2, DB}$ ) of any two sub-channels. Generally, the STCF can be computed as [20]

$$\rho_{h_{pq}^m h_{pq'}^m}(\tau) = \mathbf{E}[h_{pq}^m(t) h_{pq'}^{m*}(t - \tau)] \quad (8)$$

where  $(\cdot)^*$  denotes the operation of complex conjugate and  $\mathbf{E}[\cdot]$  represents the operation of computing expectation.

In the proposed model, the correlation characteristics of different components are discussed respectively due to the different distributions of the AAOds/EAOds and AAOAs/EAOAs: (a) In terms of the LoS component,

$$\begin{aligned} \rho_{h_{pq}^{\text{LoS}} h_{pq'}^{\text{LoS}}}(\tau) &= \frac{K}{K+1} e^{-j2\pi f_c \frac{\Delta d_{\text{LoS}}}{c}} \\ &\times e^{j2\pi f_{Tmax} \tau \cos(\alpha_T^{\text{LoS}} - \gamma) \cos(\beta_T^{\text{LoS}})} \end{aligned} \quad (9)$$

where  $\Delta d_{\text{LoS}} = \delta_R \cos(\varphi_R) \cos(\theta_R)$ .

(b) In terms of the reflection component,

$$\begin{aligned} \rho_{h_{pq}^{\text{Ref}} h_{pq'}^{\text{Ref}}}(\tau) &= \frac{\eta_{\text{Ref}}}{K+1} e^{-j2\pi f_c \frac{\Delta d_{\text{Ref}}}{c}} \\ &\times e^{j2\pi f_{Tmax} \tau \cos(\alpha_T^{\text{Ref}} - \gamma) \cos(\beta_T^{\text{Ref}})} \end{aligned} \quad (10)$$

where  $\Delta d_{\text{Ref}} = \delta_R \cos(A)$ .

(c) In the case of the single-bounced components, for the sphere model,

$$\begin{aligned} \rho_{h_{pq}^{\text{SB1}} h_{pq'}^{\text{SB1}}}(\tau) &= \frac{\eta_{\text{SB1}}}{K+1} \int_{-\pi}^{\pi} \int_{-\pi}^{\pi} e^{-j2\pi f_c \frac{\Delta d_{\text{SB1}}}{c}} \\ &\times e^{j2\pi f_{Tmax} \tau \cos(\alpha_T^{(1)} - \gamma) \cos(\beta_T^{(1)})} \\ &\times f(\alpha_R^{(1)}) f(\beta_R^{(1)}) d\alpha_R^{(1)} d\beta_R^{(1)} \end{aligned} \quad (11)$$

where  $\Delta d_{\text{SB1}} = \delta_R [\cos(\varphi_R) \cos(\beta_R^{(1)}) \cos(\theta_R - \alpha_R^{(1)}) + \sin(\varphi_R) \sin(\beta_R^{(1)})]$ , and for one elliptic-cylinder model,

$$\begin{aligned} \rho_{h_{pq}^{\text{SB2}} h_{pq'}^{\text{SB2}}}(l, \tau) &= \frac{\eta_{\text{SB2}}}{L(K+1)} \int_{-\pi}^{\pi} \int_{\beta_0^{(l)} - \beta_s^{(l)}}^{\beta_0^{(l)} + \beta_s^{(l)}} e^{-j2\pi f_c \frac{\Delta d_{\text{SB2}}}{c}} \\ &\times e^{j2\pi f_{Tmax} \tau \cos(\alpha_T^{(l,2)} - \gamma) \cos(\beta_T^{(l,2)})} \\ &\times f(\alpha_R^{(l,2)}) f(\beta_R^{(l,2)}) d\beta_R^{(l,2)} d\alpha_R^{(l,2)} \end{aligned} \quad (12)$$

where  $\Delta d_{\text{SB2}} = \delta_R [\cos(\varphi_R) \cos(\beta_R^{(l,2)}) \cos(\theta_R - \alpha_R^{(l,2)}) + \sin(\varphi_R) \sin(\beta_R^{(l,2)})]$ .

(d) In terms of the double-bounced components through the sphere model and one elliptic-cylinder model,

$$\begin{aligned} \rho_{h_{pq}^{\text{DB}} h_{pq'}^{\text{DB}}}(l, \tau) &= \frac{\eta_{\text{DB}}}{L(K+1)} \int_{-\pi}^{\pi} \int_{-\pi}^{\pi} \int_{-\pi}^{\pi} \int_{\beta_0^{(l)} - \beta_s^{(l)}}^{\beta_0^{(l)} + \beta_s^{(l)}} e^{-j2\pi f_c \frac{\Delta d_{\text{DB}}}{c}} \\ &\times e^{j2\pi f_{Tmax} \tau \cos(\alpha_T^{(l,2)} - \gamma) \cos(\beta_T^{(l,2)})} \\ &\times f(\alpha_R^{(1)}) f(\beta_R^{(1)}) f(\alpha_T^{(l,2)}) f(\beta_T^{(l,2)}) d\beta_T^{(l,2)} d\alpha_T^{(l,2)} d\alpha_R^{(1)} d\beta_R^{(1)} \end{aligned} \quad (13)$$

where  $\Delta d_{\text{DB}} = \delta_R [\cos(\varphi_R) \cos(\beta_R^{(1)}) \cos(\theta_R - \alpha_R^{(1)}) + \sin(\varphi_R) \sin(\beta_R^{(1)})]$ .

By summing over all of the above equations, we obtain the total STCF, which can be expressed as

$$\begin{aligned} \rho_{h_{pq} h_{pq'}}(\tau) &= \rho_{h_{pq}^{\text{LoS}} h_{pq'}^{\text{LoS}}}(\tau) + \rho_{h_{pq}^{\text{Ref}} h_{pq'}^{\text{Ref}}}(\tau) + \rho_{h_{pq}^{\text{SB1}} h_{pq'}^{\text{SB1}}}(\tau) \\ &+ \sum_{l=1}^L \rho_{h_{pq}^{\text{SB2}} h_{pq'}^{\text{SB2}}}(l, \tau) + \sum_{l=1}^L \rho_{h_{pq}^{\text{DB}} h_{pq'}^{\text{DB}}}(l, \tau). \end{aligned} \quad (14)$$

When we set  $\Delta d_m = 0$ , ( $m = \text{LoS, Ref, SB1, SB2, DB}$ ) in STCF, the temporal autocorrelation function (ACF) can be obtained. In the same way, the spatial CCF can be computed by setting  $\tau = 0$  [21].

## B. Doppler PSD

By the Fourier transform of the total STCF, the Doppler PSD can be obtained [19],

$$S_{h_{pq}h_{pq'}}(f_D) = \mathbf{F}\{\rho_{h_{pq}h_{pq'}}(\tau)\} = \int_{-\infty}^{\infty} \rho_{h_{pq}h_{pq'}}(\tau) e^{-j2\pi f_D \tau} d\tau \quad (15)$$

where  $\mathbf{F}\{\cdot\}$  indicates the Fourier transform,  $f_D = f_{Tmax} \cos(\theta)$  is the Doppler frequency, and  $\theta$  is the angle between the transmitting wave and the moving direction of antenna.

## C. PDP

To describe the impact of scattering on the power variation, the PDP is considered. The averaged PDP can be calculated as

$$P(\tau') = \frac{1}{N_{PDP}} \sum_{u=0}^{N_{PDP}-1} |h_{pq}(t_u, \tau')|^2. \quad (16)$$

## IV. RESULTS AND ANALYSIS

In this section, the numerical and simulation results of the channel characteristics are presented. The main parameters are chosen as follows:  $f_c = 2.075$  GHz,  $D = 2000$  m,  $R = 15$  m,  $v = 10$  m/s,  $\gamma = 0$ ,  $\theta_R = 4\pi/5$ ,  $\varphi_R = \pi/6$ ,  $\delta_R = 3$  m,  $h = 20$  m,  $L = 5$ ,  $\alpha_0^{(1)} = \pi/2$ ,  $k_{\alpha_0^{(1)}} = 5$ ,  $\beta_0^{(1)} = 0$ ,  $k_{\beta_0^{(1)}} = 20$ ,  $\alpha_0^{(2)} = \pi/4$ ,  $k_{\alpha_0^{(2)}} = 5$ .

Firstly, we investigate the ACF by setting  $\Delta d_m = 0$  in the total STCF. The results are shown in Fig. 2. For the simulation model, we assume the numbers of scatterers to be  $N_1 = 50$ ,  $N_2 = 50$ . The simulation result is computed from simulation model using correlation function in Matlab. As shown in Fig. 2, the curves of the reference model, simulation model, and simulation result match well, which demonstrates the applicability of the proposed model. On the other hand, when  $\tau$  is set to be 0 in the total STCF, we can compute the spatial CCF of two sub-channels. Fig. 3 specifies the influence of Ricean factor on CCF. When the value of  $K$  increases, the correlation between the two sub-channels becomes stronger which means enhanced spatial correlation.

In Fig. 4, the Doppler PSDs with different moving direction angles ( $\gamma$ ) of the Tx are presented. With the change of moving direction angles, the peak values of the curves also change because the Doppler shifts of the LoS components in different situations are not similar. In addition to this, when the moving direction changes, the influence from the scatterers will be different. As a result, there are some differences in the shape of the curves which show that moving direction angles have great impacts on the Doppler PSD.

Fig. 5 illustrates the comparison of PDPs between the simulation model and measurement data [3]. The channel measurement was carried out with two RX antennas placed in an harbor area and one mobile TX antenna placed on a ship. The main measurement parameters are as follows:  $f_c = 2.075$  GHz,  $v = 3.1$  m/s,  $\delta_R = 1.865$  m,  $h = 21.2$  m. In our simulation, the parameters are turned to be coincident

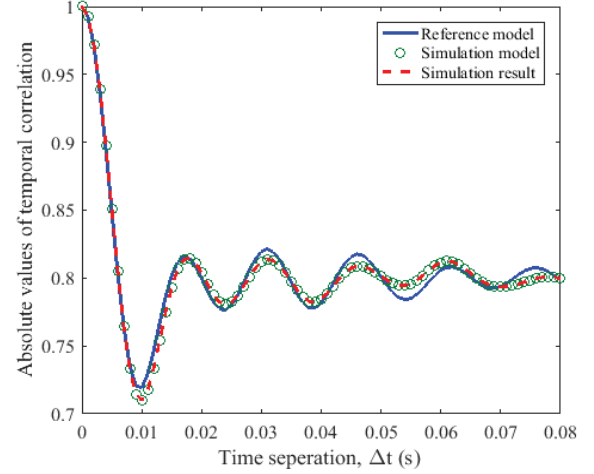


Fig. 2. The absolute values of the temporal ACFs.

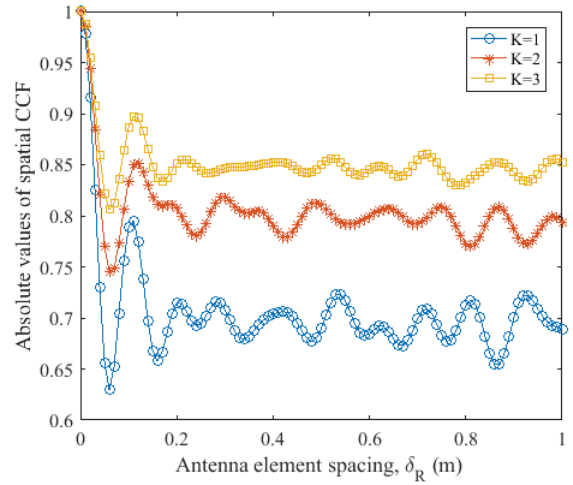


Fig. 3. The absolute values of the spatial CCFs with different Ricean  $K$  factors.

with the measurement parameters. From the result, we can see that the proposed model shows a good matching with measurement data which validates the proposed model. To verify the necessity of adopting multiple confocal elliptic-cylinder models to represent the effect of fluctuating ocean surface, a simplified model only considering the LoS component, reflection component and scattering components from the sphere model is simulated. As in Fig. 5, the simplified model can not give the enough channel information, and the effect of fluctuating ocean surface should be considered.

## V. CONCLUSIONS

In this paper, we have proposed a novel SIMO GBSM for maritime communications. It has the ability to mimic the ship-to-land channel. Based on the proposed model, the channel characteristics, such as STCF and Doppler PSD, have been illustrated. Then, we have studied the impacts of Ricean  $K$  factors on the spatial CCF and moving direction angles of the

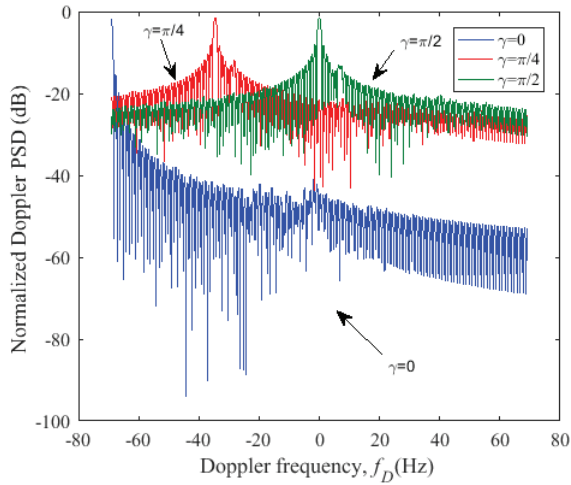


Fig. 4. The Doppler PSDs with different moving direction angles of the Tx.

Tx on Doppler PSD. The simulation results have validated the utility of the proposed GBSM. In the future, we will further investigate the impacts of more parameters and try to introduce more methods for description of the sea surface to improve the accuracy of the channel model.

#### ACKNOWLEDGMENT

This work was supported by the Natural Science Foundation of China (No. 61771293), Fundamental Research Funds of Shandong University under Grant (2017JC009), Key Research and Development Program of Shandong Province (2016GGX101014), Fundamental Research Funds of Shandong University (2017JC029), Taishan Scholar Program of Shandong Province, Science and Technology Project of Guangzhou (201704030105), EU H2020 RISE TESTBED Project (734325), National Postdoctoral Program for Innovative Talents (No. BX201700308), China Postdoctoral Science Foundation Funded Project (No. 2017M622203), and Fundamental Research Funds for the Central Universities (2242019R30001).

#### REFERENCES

- [1] S. Balkees P A, K. Sasidhar, and S. Rao, "A survey based analysis of propagation models over the sea," in *Proc. ICACCI'15*, Kochi, India, Aug. 2015, pp. 69–75.
- [2] N. Mehrnia and M. K. Ozdemir, "Multipath delay profile and Doppler spread of millimeter radiowaves over the sea channel," in *Proc. IEEE BlackSeaCom'17*, Istanbul, Turkey, Jun. 2017, pp. 1–5.
- [3] K. Yang, T. Røste, F. Bekkadal, and T. Ekman, "Experimental multipath delay profile of mobile radio channels over sea at 2 GHz," in *Proc. LAP'12*, Loughborough, UK, Nov. 2012, pp. 1–4.
- [4] J. C. Reyes-Guerrero, "Experimental broadband channel characterization in a sea port environment at 5.8 GHz," *IEEE Journal of Oceanic Engineering*, vol. 41, no. 3, pp. 509–514, Jul. 2016.
- [5] W. Wang, R. Raulefs, and T. Jost, "Fading characteristics of maritime propagation channel for beyond geometrical horizon communications in C-band," *Ceas Space Journal*, vol. 9, pp. 1–10, Dec. 2017.
- [6] J. Lee, J. Choi, W. Lee, J. Choi, and S. Kim, "Measurement and analysis on land-to-ship offshore wireless channel in 2.4 GHz," *IEEE Wireless Commun. Lett.*, vol. 6, no. 2, pp. 222–225, Apr. 2017.

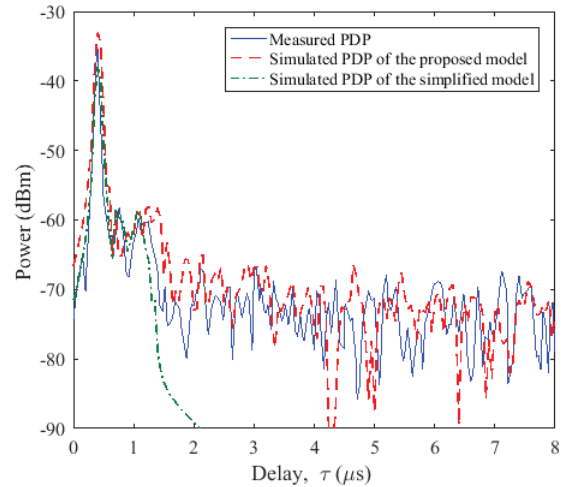


Fig. 5. The comparison of measured PDP and simulated PDP.

- [7] W. Wang, T. Jost, R. Raulefs, and U. Fiebig, "Ship-to-ship broadband channel measurement at 5.2 GHz on North sea," in *Proc. EUCAP'17*, Paris, France, May. 2017, pp. 3872–3876.
- [8] K. Yang, T. Røste, F. Bekkadal, and T. Ekman, "Land-to-ship radio channel measurements over sea at 2 GHz," in *Proc. WiCOM'10*, Chengdu, China, Sept. 2010, pp. 1–4.
- [9] K. Yang, T. Ekman, T. Røste, and F. Bekkadal, "A quasi-deterministic path loss propagation model for the open sea environment," in *Proc. WPMC'11*, Brest, France, Oct. 2011, pp. 1–5.
- [10] K. Yang, A. F. Molisch, T. Ekman, and T. Røste, "A deterministic round earth loss model for open-sea radio propagation," in *Proc. VTC'13-Spring*, Dresden, Germany, Jun. 2013, pp. 1–5.
- [11] N. Mehrnia and M. K. Ozdemir, "Novel maritime channel models for millimeter radiowaves," in *Proc. SoftCOM'16*, Split, Croatia, Sept. 2016, pp. 1–6.
- [12] I. J. Timmins and S. O'Young, "Marine communications channel modeling using the finite-difference time domain method," *IEEE Trans. Veh. Technol.*, vol. 58, no. 6, pp. 2626–2637, Jul. 2009.
- [13] J. Wang, Y. Cui, S. Ma, X. Meng, L. Liu, and J. Teng, "A non-isotropic simulation model for ship-to-ship fading channels," in *Proc. ICWMMN'15*, Beijing, China, Nov. 2015, pp. 115–119.
- [14] J. Wang, Y. Cui, S. Ma, X. Meng, and J. Teng, "A simulation model for ship-to-ship Rayleigh fading channels," in *Proc. ICSP'14*, Hangzhou, China, Oct. 2014, pp. 1692–1697.
- [15] E. Dinc and O. B. Akan, "Beyond-line-of-sight communications with ducting layer," *IEEE Commun. Mag.*, vol. 52, no. 10, pp. 37–43, Oct. 2014.
- [16] Y. H. Lee, F. Dong, and Y. S. Meng, "Near sea-surface mobile radiowave propagation at 5 GHz: Measurements and modelling," *Radioengineering*, vol. 23, no. 3, pp. 824–830, Sept. 2014.
- [17] C.-X. Wang, J. Bian, J. Sun, W. Zhang, and M. Zhang, "A survey of 5G channel measurements and models," *IEEE Commun. Surveys Tuts.*, vol. 20, no. 4, pp. 3142–3168, 4th Quart., 2018.
- [18] J. Huang, C.-X. Wang, Y. Liu, J. Sun, and W. Zhang, "A novel 3D GBSM for mmWave MIMO channels," *Sci. China Inf. Sci.*, vol. 61, no. 10, Oct. 2018.
- [19] Y. Yuan, C.-X. Wang, X. Cheng, B. Ai, and D. I. Laurenson, "Novel 3D geometry-based stochastic models for non-isotropic MIMO vehicle-to-vehicle channels," *IEEE Trans. Wireless Commun.*, vol. 13, no. 1, pp. 298–309, Jan. 2014.
- [20] Y. Liu, C.-X. Wang, C. F. Lopez, and X. Ge, "3D non-stationary wideband circular tunnel channel models for high-speed train wireless communication systems," *Sci. China Inf. Sci.*, vol. 60, no. 8, Aug. 2017.
- [21] S. Wu, C.-X. Wang, H. Aggoune, M. M. Alwakeel, and X. You, "A general 3D non-stationary 5G wireless channel model," *IEEE Trans. Commun.*, vol. 66, no. 7, pp. 3065–3078, Jul. 2018.